Characterization of Shallow Oceanic Precipitation using Profiling and Scanning Radar Observations at the Eastern North Atlantic ARM Observatory

Katia Lamer[1], Bernat Puigdomènech Treserras[2], Zeen Zhu[3], Bradley Isom[4], Nitin Bharadwaj[4], and Pavlos Kollias[3,5]

[1.] Department of Earth and Atmospheric Science, The City College of New York
[2.] Department of Atmospheric and Oceanic Sciences, McGill University
[3.] School of Marine and Atmospheric Sciences, Stony Brook University
[4.] Atmospheric Measurement and Data Sciences, Pacific Northwest National Laboratory
[5.] Department of Environmental and Climate Sciences, Brookhaven National Laboratory

Correspondence: Katia Lamer, klamer@ccny.cuny.edu

Abstract

Shallow oceanic precipitation variability is documented using 2nd generation radars located at the Atmospheric Radiation Measurement (ARM) Eastern North Atlantic observatory: The Ka-band ARM zenith radar (KAZR2), the Ka-band scanning ARM cloud radar (KaSACR2) and the X-band scanning ARM precipitation radar (XSAPR2). First, the radars and measurement post-processing techniques, including sea clutter removal and calibration against collocated disdrometer and Global Precipitation Mission (GPM) observations are described. Then, we present how a combination of profiling radar and lidar observations can be used to estimate adaptive (in both time and height) parameters that relate radar reflectivity (Z) to precipitation rate (R) in the form $Z = \alpha R^{\beta}$ which we use to estimate precipitation rate over the domain observed by XSAPR2. Furthermore, Constant Altitude Plan Position Indicator (CAPPI) gridded XSAPR2 precipitation rate maps are also constructed.

Hourly precipitation rate statistics estimated from the three radars differ; that is because KAZR2 is more sensitive to shallow virga and because XSAPR2 suffers from less attenuation that KaSACR2 and as such is best suited to characterize intermittent and mesoscale-organized precipitation. Further analysis reveals that precipitation rate statistics obtained by averaging 12h of KAZR2 observations can be used to approximate that of a 40-km radius domain averaged over similar time periods. However, it was determined that KAZR2 is unsuitable to characterize domain average precipitation rate over shorter periods. But even more fundamentally, these results suggest that these observations cannot produce objective domain precipitation estimate and that the simultaneous use of forward-simulators is desirable to guide model evaluation studies.

1.0 Introduction

Characterizing shallow oceanic precipitation is all-important to improving our understanding of shallow cloud systems since precipitation is related to a number of cloud process all of which may affect cloud properties. For example, precipitation leads to a reduction in the droplet number via the collision-coalescence process and of the liquid water path through sedimentation. Furthermore, a number of modeling studies have suggested that drizzle organization, intensity and subcloud layer evaporation could play a role in organizing stratocumulus cloud decks on the mesoscale (Zhou et al., 2017; Savic-Jovcic and Stevens, 2008; Wang and Feingold, 2009; Yamaguchi and Feingold, 2015; Zhou et al., 2018). Ultimately, these controls may alter low cloud radiative properties and climate (Wood, 2012). Quantification, over a domain of several kilometers, of marine drizzle cell precipitation rate and environmental conditions, could provide additional observational constrains for modeling studies. Unfortunately collecting such observations remain challenging over the ocean.

Although satellite-based microwave sensors can infer the spatial distribution of liquid water path (Wood and Hartmann, 2006; Miller and Yuter, 2013) and precipitation rate (Ellis et al., 2009; Adler et al., 2009; Rapp et al., 2013) they have poor horizontal resolution and suffer from surface inference causing them to under sample the cloud field variability and to underreport boundary-layer cloud and precipitation occurrence (Schumacher and Houze Jr, 2000; Rapp et al., 2013). In contrast, airborne (Stevens et al., 2005; Wood et al., 2011; Moyer and Young, 1994; Vali et al., 1998; Paluch and Lenschow, 1991; Sharon et al., 2006) and ship-based (Yuter et al., 2000; Comstock et al., 2005; Feingold et al., 2010) sensors can resolve the spatial/temporal variability of the cloud and precipitation field, but field campaigns deploying such sensors are often expensive to conduct and limited in temporal duration (Stevens et al., 2003; Bretherton et al., 2004; Rauber et al., 2007). Island-based observatories such as the U.S. Department of Energy (DOE) Atmospheric Radiation Measurement (ARM) Eastern North Atlantic observatory (ENA, Mather et al., 2016; Kollias et al., 2016) and the Barbados Cloud Observatory (BCO, Lamer et al., 2015; Stevens et al., 2016) operating profiling and scanning remote sensors can provide long-term statistics of marine light precipitation.

Beyond detecting, quantifying the spectrum from drizzle to rain from warm clouds is especially challenging since at small drizzle rates the droplets they contain are mostly spherical and as such do not generate the typical polarimetric signals required of common precipitation rate retrievals (e.g., Villarini and Krajewski, 2010; Gorgucci et al., 2000). As an alternative to polarimetric signatures, a combination of sensors is typically required to retrieve precipitation rate (R); Combinations of radar reflectivity (Z) and in-situ measurements have led to the development of Z-R relationships (Wood, 2005; Comstock et al., 2004; VanZanten et al., 2005; Vali et al., 1998) however, these tend not to be universally applicable since they are based on assumptions about the drizzle particle size distribution which may vary with factors such as aerosol loading and liquid water path. Moreover, relying on surface disdrometer measurements to characterize warm precipitation may be especially unsuitable at the ENA where i) a large fraction of the precipitation does not reach the surface (Yang et al., 2018), ii) precipitation reaching the ground typically does so with an intensity below the detection limit of most optical-based disdrometers (~10^{-2} mm hr^{-1}) and iii) evaporation is an active process such that water drop size distribution information retrieved at one height may not be appropriate to represent the entire atmospheric column.

Alternatively, a method combining radar reflectivity and lidar backscatter measurements has been proposed to retrieve *R* with fewer assumptions about the drizzle particle size distribution (Intrieri et al., 1993; O'Connor et al., 2005); Because of the current rarity of scanning lidar observations, this technique has only been used to retrieve *R* in the column and cannot be used to address the concerns present in recent studies suggesting that scanning systems are essential to map domain properties (Oue et al., 2016).

Here we propose to exploit the availability of collocated vertically-pointing radar and lidar as well as scanning radar systems to characterize marine precipitation rate variability over a domain of 40-60 km around the ENA observatory. The Eastern North Atlantic region, with its abundance of marine boundary layer precipitating clouds, is an ideal location for such study (Rémillard and Tselioudis, 2015; Wood, 2012).Observations from the Ka-band ARM Zenith Radar (KAZR2) and zenith-pointing ceilometer lidar are combined to estimate adaptive (both in time and height) *Z-R* relationships which we then use to estimate precipitation rate across the domain observed by the X-band Scanning ARM Precipitation Radar (XSAPR2). Domain-average and time-average precipitation rate estimates obtained from zenith-pointing and scanning observations are compared to document the complementarity and applicability of each sensor in documenting precipitation rate from warm boundary layer clouds.

2.0 Eastern North Atlantic Observatory

In October 2013, the ARM program established a permanent observatory in the Eastern North Atlantic on the island of Graciosa (~60 km^2 area; 39.1°N, 28.0°W). The site, located within the Azores archipelago, straddles the boundary between the subtropics and the midlatitudes and as such is subject to a wide range of different meteorological conditions including periods of relatively undisturbed trade-wind flow, midlatitude cyclonic systems and associated fronts, and periods of extensive low-level cloudiness (Rémillard and Tselioudis, 2015). The observatory hosts an extensive instrument suite including three second generation radar systems: The Ka-band ARM Zenith Radar (KAZR2), the dual-frequency Ka-and W-band Scanning ARM Cloud Radar (SACR2) and the X-band Scanning ARM Precipitation Radar (XSAPR2) which's specifications are listed in Table 1. A short description of the radar systems is provided here with emphasis on changes in configuration from the first to the second generation.

2.1 KAZR2

KAZR2 operates at 34.8 GHz (λ = 8.6 mm) and is an upgraded version of the KAZR that replaced the ARM MilliMeter Cloud Radar (MMCR, Kollias et al., 2016). KAZR2 uses an Extended Interaction Klystron (EIK) amplifier with a 2.2 kW peak power and 5 % duty cycle. Its dual receiver configuration allows for the simultaneous transmission of two pulses: i) A long (4 μs) pulse with frequency modulation (pulse compression) for higher sensitivity (~-44 dBZ at 1 km not considering signal integration gain) at ranges from 737 m from the radar to 18 km and ii) A short pulse (200 ns) with a sensitivity of (~-32.5 dBZ at 1 km not considering signal integration gain) at ranges from 72 m to 18 km from the radar. KAZR2 has a narrow (0.3°) 3-dB antenna bandwidth and is nominally operated with a range resolution of 30 m, a temporal resolution of 2 sec and is set to record the full radar Doppler spectrum with 256 or 512 FFT points. KAZR2 transmits a horizontal pulse and receives both horizontal and vertical polarization such that the

only polarimetric information it can measure is linear depolarization ratio.

2.2 KaSACR2

KaSACR2 is a fully polarimetric radar that operates at 35.3 GHz (λ = 8.5 mm) and is an upgraded version of the single polarization KaSACR described in Kollias et al., (2014a,b). The KaSACR2 also uses an EIK amplifier with a 2.2 kW peak power, has a 5 % duty cycle and a 3-dB antenna beamwidth of 0.3°. Currently, it is operated with a short pulse, although it could be operated with a longer pulse with pulse compression for increased sensitivity. Owing to its narrow beam width KaSACR2 must scan rather slowly (3-6° s^{-1}) to collect observation with a sensitivity of ~-15 dBZ at 20 km (not considering signal integration gain). The KaSACR2 conducts a cloud sampling strategy that includes different modes (Kollias et al., 2014a,b). Here, because of our interest to map precipitation structure and rate over a large horizontal domain, we only use observations collected in Plan Position Indicator (PPI) configuration only available at 0.5° elevation angle over a 160° wide azimuth sector. The KaSACR2 conducts a PPI scan every 15 min and takes 2 min to collect each PPI. The KaSACR2 employs frequency hopping and staggered pulse repetition time techniques to mitigate artifacts due to second trip echoes and velocity aliasing; This however comes at the expense of preventing the collection of the full Doppler spectrum.

2.3 XSAPR2

XSAPR2 operates at 9.5 GHz (λ = 3.2 cm); It is an upgraded version of the XSAPR as it operates with an improved digital receiver and a larger antenna (5 m) which results to an exceptionally narrow 3-dB antenna beamwidth of 0.45°. The requirement for the XSAPR2 to have a narrow antenna beamwidth emerged from two main needs: i) To reduce the impact of sea-clutter at low-elevations and ii) maintain high angular resolution over a 60 km radius in order to resolve small scale oceanic precipitating clouds. XSAPR2 uses a high-power Magnetron with a 300kW peak power and a maximum duty cycle of 0.1 %. Under nominal operational conditions, the XSAPR2 transmits a 60 m long pulse and scans at a relatively slow rate (6° s^{-1}) to collect observations with a sensitivity of ~-21 dBZ at 20km (not considering integration gain). The XSAPR2 volume coverage pattern (VCP) scan strategy consists of a series of PPI scans every 0.5° elevation between the angles of 0° and 5°. Because of considerable beam blockage in the southerly direction a 160° azimuth sector coverage is achieved. The VCP scan (i.e. the entire set of PPI scans) is completed within 5 min and subsequently repeated. Horizontal and vertical polarization are possible for both transmit and receive states, meaning XSAPR2 collects a full suite of polarimetric variables while in scanning mode.

3.0 Radar Observations Post-Processing

Radar observations require considerable post-processing for the removal of non-meteorological targets before they can be scientifically interpreted or used to retrieve geophysical quantities such as precipitation rate. Radar data post-processing is described in section 3.1 and cross-comparison between different systems for calibration is described in section 3.2. Note that the KAZR2 data used for analysis are from "enakazrgeC1.a1" files, KaSACR2 data are from

"enakasacrppivhC1.a1" files and the XSAPR2 from the "enaxsaprsecD1.00 files". All data files were obtained from the ARM archive (https://www.archive.arm.gov/discovery/).

3.1 Removal of Non-Meteorological Targets

First, signal processing artifacts (e.g. second trip echoes) and echoes of non-meteorological origin (e.g., biological echoes, sea-clutter, and ground-clutter) are identified and removed.

The KaSACR2 system operates in fully polarimetric mode and uses staggered pulse repetition time and frequency hopping to automatically remove second trip echoes, perform velocity dealiasing and increase the number of independent samples (Pazmany et al., 2013). The XSAPR2 systems operates using a magnetron system which is coherent on receive (i.e., transmitted pulse phase is random). For the XSAPR2, the removal of second trip echoes is done using Normalized Coherent Power (NCP) which is the coherency of the received pulse with respect to the last transmitted pulse. For atmospheric echoes within maximum unambiguous range, NCP is high since the radar receiver is phase-locked to the phased of the last transmitted pulse. Outside of the maximum unambiguous range, NCP is low since the radar receiver has already phase-locked on the phase of another transmitted pulse. Here, an NCP threshold of 0.3 is used to identify echoes originating from outside the maximum unambiguous range (i.e. second trip echoes).

Biological targets such as insect and birds often contaminate radar observations especially over land (e.g., Luke et al., 2008). Their occurrence varies with atmospheric condition, time of the year, and time of the day (Alku et al., 2015). KAZR2 observations at the ENA seem minimally impacted by biological echoes. Furthermore, the fact that the bulk of the KaSACR2 and XSAPR2 observations are collected over open ocean and that Graciosa is a small island suggests that biological targets should not be a concern at this particular location.

On the other hand, low elevation angle observations are susceptible to sea-clutter contamination. Research on radar sea-clutter characterization and remediation has been ongoing for over 20 years (e.g., Horst et al., 1978; Gregers-Hansen and Mital, 2009; Nathanson et al., 1991); Observational and modeling studies suggest that factors such as oceanic wave properties (related to local wind speed and direction), swell and air density streams can affect sea-clutter occurrence. Radar characteristics such as wavelength, wave polarization, beam width and grazing angle are also known to affect sea-clutter characteristics, amounts and our ability to isolate atmospheric returns from sea-clutter. Here, observations collected over a range of wind conditions during nearly 100 hours of clear sky conditions are used to examine how sea-clutter characteristics vary with radar wavelength, beam width and beam elevation angle.

First, the distribution of sea-clutter reflectivities as measured by the XSAPR2 and KaSACR2 at elevation 0.5° are compared to document the antenna beam width effect (Fig. 1d). The KaSACR2 (0.3° 3-dB antenna beam width) sea-clutter reflectivity distribution is narrower with a peak at -21 dBZ and a majority of echoes below -15 dBZ (Fig. 1d black line) while the XSAPR2 (0.45° 3-dB antenna beam width) sea-clutter reflectivity distribution is wider, peaks at -18 dBZ and covers a range from -40 dBZ to +10 dBZ (Fig. 1d red line). This can be explained by the XSAPR2 wider antenna beam width which results in a larger fraction of the radiated energy to hit ocean waves, causing higher ocean clutter return power. Similar to beam width, elevation angle affects how

much sea is in the radar field of view and the spatial extent of observed sea-clutter. Figure 1d, shows that, at 1.0° elevation, XSAPR2 sea-clutter reflectivity peaks at a lower reflectivity of -25 dBZ (blue line) and Fig. $1b_3$ shows that in this configuration it frequently (> 25 % of the time) detects clutter only over a domain of 10 km radius around the site which is much less than it detects when collecting observations at 0.5° elevation (significant clutter in a 20 km radius around the site Fig. $1a_3$).

Now that we have characterized sea-clutter intensity and frequency of occurrence using clear sky observations, we next evaluate its impact on the detection of meteorological targets using observations containing mixture of hydrometeor and sea-clutter. To isolate hydrometeors from clutter, we exploit the correlation coefficient ρ_{HV} which we know is affected by the relative occurrence of signal to clutter; ρ_{HV} is typically close to 1 for liquid-phase hydrometeors and lower for non-meteorological targets. Looking at KaSACR2 reflectivity and ρ_{HV} confirms that at Ka-band wavelength the signal to clutter ratio is high and hydrometeors contributions dominate both radar reflectivity and correlation coefficient measurements (Fig. $1c_1$ and $1c_2$, respectively). The enhanced KaSACR2 signal-to-clutter ratio is attributed to two effects: i) its narrow beamwidth which causes a smaller fraction of the transmitter energy to hit the sea surface and ii) its shorter wavelength which creates a larger distinction between hydrometeor scattering - which follow Rayleigh scattering $\sim 1/\lambda^4$ - and sea-clutter scattering – which follow $\sim 1/\lambda$. Using KaSACR2 observations has a guide to locate cloud and precipitation location (Fig $1c_1$), it is apparent that it is not possible to distinguish atmospheric signals from sea-clutter in XSAPR2 radar reflectivity observation collected at 0.5° (Fig. $1a_1$).

Several techniques that use both time-domain and frequency domain filtering methods have been proposed to discriminate between sea-clutter and meteorological targets in precipitation radar observations (e.g., Torres and Zrnic, 1999; Siggia and Passarelli, 2004; Nguyen et al., 2008; Alku et al., 2015). Ryzhkov et al. (2002) present an echo classification technique based on fuzzy logic and a multiparameter dataset including radar reflectivity, mean Doppler velocity, spectrum width, differential reflectivity, differential phase, linear depolarization ratio, and cross-correlation (ρ_{HV}). In the current study, given the radars narrow beam width and short wavelength, an approach solely based on ρ_{HV} is used to filter sea-clutter. Since cross-correlation between horizontal and vertical cross-polar received powers is largest for spherical hydrometeors, we label observations with ρ_{HV} larger than a certain threshold as atmospheric returns and the rest as sea-clutter. The analysis of a large sample of ρ_{HV} observations during clear and cloudy sky conditions indicates that the use of a threshold of 0.9 for KaSACR2 and an average (over 5 range gates and 5 azimuthal measurements) threshold of 0.55 for the XSAPR2 can be used to isolate hydrometeor-dominated from clutter-dominates observations. The proposed ρ_{HV} technique successfully isolates atmospheric returns at the same location for both the X-band at 1.0° elevation and the reference Ka-band 0.5° elevation (Fig. $1b_2$ and c_2 respectively; pink regions). However, it only identifies a fraction of the atmospheric returns in the X-band 0.5° elevation observations. There, additional filtering, beyond the scope of this study, would be required to suppress the remaining sea-clutter and recover the missing atmospheric returns (see Moisseev and Chandrasekar, 2009; Unal, 2009 who propose advanced technique). Given this, XSAPR2 cross validation and precipitation rate maps will be estimated using observations collected at 1.0° elevation since it offers the best compromise between proximity to the surface and minimum sea-clutter contamination.

3.2 Radar Calibration

Calibrated reflectivity observations are necessary to perform quantitative precipitation rate retrievals. Following Kollias et al. (2019), KAZR2 calibration is performed using collocated surface-based Parsivel laser disdrometer equivalent radar reflectivity estimates during light precipitation events as well as CloudSat observations collected over a small radius around the site. We estimate that, during the period of interest (01/10/2018 to 04/01/2018), KAZR2 radar reflectivity measurements are off by about +3-dB which we proceeded to correct for. The detailed time-series of KAZR2 calibration offset is presented in Fig. 2a.

Comparison of total (Fig. 3a) and range resolved (Fig. 3b) histograms of radar reflectivity measured by KAZR2 (pre-calibration) and KaSACR2 at zenith confirm that during the analysis period the KaSACR2 matched KAZR2. For this reason, KaSACR2 radar reflectivity measurements were also adjusted by the calibration constant depicted in Fig. 2a. Note how this comparison between the KAZR2 and KaSACR2 was performed between 1.5 to 5 km to avoid any differences in the reported radar reflectivities due to differences in how they detect ground/sea-clutter.

Calibrating the XSAPR2 radar reflectivity measurements is more challenging since it does not perform profiling observations and as such it cannot be benchmarked against disdrometer and KAZR2 observations. Performing a physical subsystem calibration remains the best way to calibrate the XSAPR2 system. Prior to the ACE-ENA field campaign (06/2017) the ARM engineering team performed such a procedure which is expected to bring the calibration of the XSAPR2 system used in this study to within 1 dB. Here, in an effort to develop alternative calibration/cross-validation methods, we also compare the XSAPR2 radar observations to Global Precipitation Measurement (GPM) Ku-band frequency of the Dual-frequency Precipitation Radar (DPR) observation when the satellite track crosses within a 245 km radius of the XSAPR2 radar site. It is not expected that both sets of observations will perfectly match because of the different footprints, path lengths and surface returns of both radars but this comparison should at least provide some insight in the event that the difference between both sensors is larger than several dB. For the comparison, the ground-based XSAPR2 reflectivity measurements are smoothed and interpolated to the satellite sampling volume: The azimuth-range measurements are smoothed using the 0.71° 3-dB beamwidth antenna weighting function of the GPM DPR (5-km footprint). Nearest neighbor is then used to match the satellite measurements in the horizontal plane while linear interpolation is used to match them in the vertical plane (Warren et al., 2018). Matched XSAPR2 radar reflectivity measurements are compared to GPM DPR corrected reflectivity measurements (GPM product version V06A Iguchi et al., 2010). Considering differences in radar sensitivity, radar reflectivity measurements with returns smaller than 14 dBZ are not considered during the comparison procedure (Toyoshima et al., 2015) and only periods when both radars coincidently detect significant precipitation are used to perform calibration. For the analysis period, a total of 3 GPM overpasses with significant precipitation were observed for a total number of 1516 data points for the comparison.

An example of concurrent XSAPR2 and GPM DPR radar reflectivity observations are shown in Fig. 4a and c respectively. The example shows that both radars detected several shallow precipitation cells with cloud top heights between 3 and 4 km (Fig. 3b). Beyond agreeing in the

location of these precipitation echoes, both radars (XSAPR2 and GPM DPR) are found to agree on their reflectivity intensity. To confirm their agreement, we estimated Contour of Frequency by Altitude Diagram (CFAD) of the differences in radar reflectivities between the matched XSAPR2 and GPM DPR for all 1516 available observations (Fig. 4b). Above the height at which GPM DPR is known to suffer from surface echo contamination (i.e., 1.5 km), the comparison between XSAPR2 reflectivities and GPM DPR reflectivities shows no noticeable difference (i.e., no bias). A scatter plot between the matched GPM DPR and XSAPR2 radar reflectivity for height above 1.5 km confirms the overall lack of bias beyond the expect 1 dB between the two radars at all reflectivity (Fig. 4d on which the orange line depicts the best fit to the data and the dashed line represent a perfect match between the datasets and the grey shading indicates the data density). As mentioned above, scatter is expected because of the differences in configuration of both radar systems. The cloud types present in the cases available could further enhance the impact of the radar system differences since the shallow clouds observed during the 3 overpasses are of similar or even smaller size compared to the GPM DPR footprint. Small clouds could lead to non-uniform beam filling issue and as such to the GPM DPR underestimating the reflectivity of these cloud system which could partially explain the seemingly "high" bias of the XSAPR2 in Fig. 4d. Knowing that the ARM engineering team had calibrated the XSAPR2 just before the observations used here were collected and because this comparison with the GPM DPR showed no bias larger than several dB, we conclude that, for the observation period between 01/10/2018 to 04/01/2018, the XSAPR2 was reasonably well calibrated and does not require any radar reflectivity adjustments.

4.0 Radar Reflectivity-Based Precipitation Rate Retrievals

4.1 KAZR2

Intrieri et al. (1993) and later O'Connor et al. (2005) proposed a technique to constrain water drop size distribution using lidar backscatter (related to water drop cross-section) and radar Doppler spectral width (related to the width of the water drop size distribution). This radar-lidar technique can be used to estimate precipitation rate at all levels in the subcloud layer when collocated radar and ceilometer observations are available. We apply this technique to the vertically pointing ceilometer lidar and KAZR2 pair operating at the ENA. The O'Connor et al. (2005) technique requires ceilometer backscatter to be calibrated and remapped to the radar spatio-temporal resolution (here 2 s x 30 m). Ceilometer backscatter is calibrated following a variation of the O'Connor et al. (2004) technique by scaling observed path-integrated backscatter in thick stratocumulus to match theoretical cloud lidar ratio values. Satisfactory conditions for ceilometer backscatter calibration are identified as the first (in time) 20-min periods each day with standard deviation of lidar ratio smaller than 1.5. The observed backscatter during the "satisfactory 20-min period" are input to Hogan (2006)'s multi scattered model to determine a daily backscatter calibration factor. For days where satisfactory conditions are not observed, a climatological calibration factor of 1.35 is used to calibrate the observed backscatter. For the current analysis period, the ceilometer backscatter calibration constant was estimated to vary around 1.35+/- 0.08. (Fig 2b). Calibrated ceilometer backscatter is subsequently mapped on the KAZR2 time-height grid using a nearest neighbor approach.

This radar-lidar technique generates time-height maps of precipitation rate from 200 m above

ground level to 90 m below cloud base height which are filtered for aerosol contamination. We use the clear-sky – according to KAZR - calibrated lidar backscatter signals as a reference for aerosol behavior. Lidar calibrated backscatter values below the mean clear-sky calibrated backscatter value at each height, depicted as the black vertical line in Fig. 2c, are systematically removed from the analysis to leave only drizzle signals. In addition to aerosol contaminated returns, unphysical values with median diameter smaller than 10 μ m or equal or large to 1000 μ m are also removed from our analysis.

Two one-hour examples of cloud location (black dots) and precipitation rate estimated using this technique are shown in Fig. 5a and b. Because of evaporation, the most intense precipitation rates are observed near cloud base height and a significant fraction of the precipitation does not reach the surface and falls as virga.

4.2 XSAPR2

As previously mentioned, the estimation of the precipitation rate for the XSAPR2 i) cannot depend on the use of polarimetric observations, because of the absence of polarimetric signature from spherical drizzle drops and ii) cannot depend on the use of disdrometer-based estimates of the relationship between the radar reflectivity (Z) and the precipitation rate (R), because observations collected at the surface may not be representative of other levels in the subcloud layer especially at the ENA where evaporation is an active process.

To accommodate changes in drizzle drop size distribution with height which could be associate for example to changes in aerosol loading or evaporation, we propose to construct adaptive (both with time and height) Z-R relationships in the form $Z = \alpha R^{\beta}$ from precipitation rates retrieved through the KAZR-ceilometer technique (see section 4.1). Every 30 min, independently for every level in the subcloud layer, retrieved zenith precipitation rates (R in mm hr^{-1}) and calibrated KAZR reflectivity (Z in mm^6 m^{-3}) reported during a 12-h window around that time are related through the relationship:

$$\log_{10}(Z) = log_{10}(\alpha) + \beta \cdot log_{10}(R) \quad (1)$$

The prefactor α and exponent β are estimated using a total least square regression technique only considering R between $10^{-3.5}$ and $10^{0.5}$ mm hr^{-1} and only if at least 350 precipitation detections are available. When too few observations are available, average (for the period of the current study) α and β are used. A 12h time window was determined to be the best compromise between data density and least change in water drop size distribution characteristics.

To evaluate the adaptive Z-R, we apply three different precipitation retrieval techniques to KAZR2 reflectivity observations: We compare precipitation rate statistics retrieved following the O'Connor et al. (2005) technique (ideal technique, red), to those estimated using Z-R relationships constructed using fixed (approach proposed by Comstock et al. (2004), green) or adaptive (approach proposed here, black) coefficients (presented in Fig. 6e and f respective). Figure 6f shows that the proposed adaptive Z-R relationships can reproduce the precipitation rate statistics obtained using the ideal O'Connor et al. (2005) technique. The same cannot be said from using traditional fixed Z-R relationships such as that proposed by Comstock et al.

(2004) which tends to create an underestimation of precipitation intensity (Fig. 6e).

Fig. 6a and b respectively present time series of α and β near cloud base (i.e., 90 m below cloud base height) for a 30-day long period that overlaps with the second phase of the ACE-ENA field campaign: Again for comparison we illustrate our adaptive coefficients (black), the Comstock et al. (2004) constant coefficients (dashed green) and coefficients estimated from surface-based Parsivel laser disdrometer measurements (dashed orange). The gradual increase in both the adaptive α and β coefficients over time is consistent with reports of observed conditions indicating a transition from shallow precipitation at the end of January to deep frontal precipitation at the end of February. CFADs of α and β (Fig. 6c and d respectively) show how the adaptive α additionally has a tendency to increase with distance from cloud base (from top to bottom), which is consistent with the evaporation of small drops that leads to an increase in mean drop size and has been previously reported by Comstock et al. (2004) and discussed in VanZanten et al. (2005).

Figure 5c and d show how, by applying the adaptive *Z-R*, XSAPR2 reflectivity observations collected at 1° elevation can be converted to precipitation rate. Note how the adaptive *Z-R* relationships were directly applied to clutter-filtered calibrated XSAPR2 radar reflectivity measurements since we estimate that, for the majority of the conditions occurring at the ENA observatory, both two-way gas attenuation and liquid attenuation at X-band are negligible; According to Rosenkranz (1998), at X-band frequency, gas attenuation generally amounts to 0.03 dB km^{-1} which is much smaller than even the radar calibration uncertainty. Similarly, Matrosov et al. (2005) discusses how, for rain rates of 2 mm hr^{-1}, liquid attenuation roughly amounts to 0.015 dB km^{-1} which over the depth of the shallow systems producing this type of precipitation cumulates to liquid attenuation less than 1 dB again within the radar calibration uncertainty. We do however acknowledge that, for deep convective systems, liquid attenuation correction would be granted, but since this type of precipitating system was not being frequently observed at the ENA observatory, we did not apply any liquid attenuation correction to the XSAPR2 measurements.

4.3 KaSACR2

Before quantitatively estimating precipitation rate from KaSACR radar reflectivity measurements, we also consider how its wavelength responds to the presence of atmospheric gases. Rosenkranz (1998) propagation model suggests that, for the conditions observed at the ENA, two-way gas attenuation of Ka-band signals can amount to 0.25 dB km^{-1}. Although this may seem small and can be insignificant when collecting observations of boundary layer clouds in profiling mode, in scan mode, attenuation of Ka-band reflectivity by atmospheric gas can amount to 10 dB at 40 km range (Fig. 7b difference between the black and green curve) and as such should not be neglected. Also note that in addition to the gaseous attenuation, Ka-band radars suffer from considerable liquid water attenuation. According to Matrosov (2005), the relationship between one way liquid attenuation a (dB km^{-1}) and precipitation rate R (mm hr^{-1}) is very robust ($a = 0.28R$). His findings were verified using Mie scattering calculations on all particle size distributions observed by the ENA Parsivel laser disdrometer. The top panels of Fig. 8 illustrates an example of observations collected by the KaSACR at 0.5 elevation on 02/13/2018. In this example, liquid contributed anywhere from 2 to 10 dB in total attenuation at Ka-band over the 40 km observation domain (Fig. 8e). If left uncorrected, liquid attenuation

459 can lead to errors in preciptiation rate estimates up to 3 mm hr^{-1} in this example (Fig. 6f). The
460 bottom panels of Fig. 8 also shows reflectivity and precipitation rate for the XSAPR2 which,
461 as discussed in the previous section, only suffers from negligible attenuation. With the caveat
462 that we are comparing rain rates retrieved at slightly different slanted elevations, comparing
463 rain rates retrieved from the XSAPR2 observations (Fig. 8h) and from the KaSACR2
464 observations corrected for both gas and liquid attenuation (Fig. 8d) also highlights the fact that
465 even after all correction are performed the KaSACR2 "realized" sensitivity does not allow it
466 to detect some of the precipitation the more sensitive XSAPR2 can detect. The range-
467 dependent sensitivity of both sensors can be contrasted in Fig. 7b.
468
469 **5.0 Complementary of different radar systems in Characterizing Light Precipitation**
470 **Variability**
471
472 As discussed in section 2.0, the KAZR2, KaSACR2 and XSAPR2 radars sample light
473 precipitation using very different transmission and sampling strategies. In this section we highlight
474 some of the advantages and tradeoffs of using each radar system to characterize different aspects
475 of light precipitation variability.
476
477 First constrasting the two scanning radar XSAPR2 and KaSACR2. Although the Ka-band
478 SACR2 experiences less sea-clutter than the X-band SAPR2, because of needs for cloud
479 sampling, it only currently performs one PPI scan at 0.5° every 15 min which limits its
480 temporal resolution. In addition, based on their technical specifications (Table 1), the XSAPR2
481 single pulse radar sensitivity is approximately 10 dB higher than that of the KaSACR2 (Fig. 7b
482 blue and black line respectively). Finally, the Ka-band SACR2 also suffer from significantly more
483 attenuation from atmospheric gases (Fig. 7b green line) and liquid water which even if corrected
484 for still decrease it's "realized" sensitivity. For all these reasons, we conclude that the XSAPR2
485 is more suitable for characterizing light precipitation variability over large domains.
486
487 Second, to contrast the XSAPR2 and KAZR2, we compare, over the course of 36 hours between
488 00:00 UTC February 2 and 12:00 UTC February 3, hourly precipitation rate variability in the forms
489 of frequency of occurrence in different precipitation rate bins (pdf). Figure 9a shows estimates
490 from the scanning XSAPR2 collecting observation in PPI mode covering a domain between 2.5
491 and 40 km at 1° elevation thus transecting heights between ~100 m and 750 m (also refer to Fig.
492 7a to visualize the XSAPR2 sampling geometry). Figure 9b and c respectively show estimates
493 from the vertically pointing KAZR2 200 m above the surface and 90 m below cloud base which
494 was around 850 m.
495
496 From Fig. 9b and c, it is evident that KAZR2, with its high sensitivity, is especially well suited to
497 document light precipitation and drizzle falling at a rate as low as 10^{-4} mm hr^{-1}. KAZR2
498 observations show a reduction in the number of precipitation events and in precipitation intensity
499 from cloud base (Fig. 9c) towards the surface (Fig. 9b). This supports previous hypothesis that at
500 the ENA a large fraction of the light precipitation falls in the form of virga (Ahlgrimm and Forbes,
501 2014; Yang et al., 2018). Under these circumstances, where the character of precipitation changes
502 dramatically with height and its intensity is very low (below 10^{-3} $mmhr^{-1}$), scanning radar
503 observation at a fixed elevation may become inadequate to characterize surface precipitation over
504 a large domain owing to Earth curvature effects. Fig. 7a illustrates the height above the surface of

a 1° elevation scan with distance away from the radar; at a distance of 10-20 km the radar beam is already 250 m above the surface while at a distance of 20-30 km this same radar beam is now 500 m from the surface. This non-uniformity of the radar beam height with distance makes scanning cloud radar observations at one elevation angle more adequate to document the character of vertically uniform precipitation. The rapid sampling rate of the KAZR2 also allows it to describe the vertical structure of precipitation variability at a high temporal (scales as short as 2s).

On the other hand, one drawback of vertically pointing KAZR2 observations is that they are limited to sampling only those precipitation events advected overhead. It is not uncommon to temporally average vertically pointing observation to create a proxy for domain average statistics, however as depicted in Fig. 5 it may be difficult to address the domain representativeness of one-hour of vertically pointing precipitation rate estimates. It can also be challenging to interpret the mesoscale organization of the precipitation field using vertically pointing observations alone; Scanning systems such as the XSAPR2 can help fill this gap. Figure 5c and d show XSAPR2 1° elevation PPI scans collected at 10:00 am and 8:00 am respectively which corresponds to the center time of the KAZR2 time-height observations presented in Fig. 5a and b. XSAPR2 can observe the structure and scales of popcorn precipitation and squall line precipitation over a domain of roughly 2,500 km^2. In its current configuration, the XSAPR2 system can be used to document the horizontal structure and temporal variability of light-to-moderate precipitation on scales of ~5 minutes. Referring back to Fig. 9a hourly precipitation rate pdfs, it is evident that by covering a larger domain XSAPR2 is able to observe a larger number of near surface sporadic precipitation events such as that observed on Feb 03 around 0:00 and of isolated deep convective events responsible for more intense precipitation ($R > 3$ mm hr^{-1}) such as that observed on Feb 03 around 8:00.

6.0 Gridded Domain Precipitation Rate Estimation

One way for scanning radars to overcome some of the limitation of their scanning strategy is to develop horizontal, two-dimensional, gridded maps of the radar observables and other quantities (i.e. precipitation rate) using measurements collected at different elevations angles (i.e., construct constant altitude plan position indicator (CAPPI) maps). Here, gridded XSAPR2 CAPPI's are constructed as follows: We perform the polar to Cartesian transformation for each individual reflectivity measurement using a standard atmosphere radio propagation model which considers the height of the beam above the Earth surface, and the distance between the radar and the projection of the beam along the Earth surface (Doviak and Zrnic, 1993). Using these Cartesian coordinates each PPI is mapped on a 100 m horizontal grid for which each grid point is populated using a triangulation technique (i.e., the nearest three observations are linearly interpolated to populate the grid cell). Then, every 100 m in the horizontal, a grid point at constant altitude is populated by i) a measured value if falling on an elevation where observations were collected or otherwise ii) a weighted average of the gridded data from the three closest PPI; The weight being the inverse horizontal distance from the grid location. The aforementioned adaptive *Z*-*R* relationships are then applied to the Cartesian grid reflectivity observations to produce precipitation rate CAPPI. Note that producing an unbiased assessment of precipitation rate over the domain covered by the scanning radar would require the application of a uniform sensitivity threshold over the entire domain. The need for such a threshold creates a tradeoff between

551 documenting a large domain and documenting weak precipitation events. As quantified in Fig. 7b,
552 at a distance of 40 km the XSAPR2 is only capable of detecting precipitation events of intensity
553 larger than $10^{-2.8}$ mm hr^{-1} and any desire to document weaker precipitation rate events would
554 further limit domain size.
555
556 **7.0 Domain Average Precipitation Rate - When do Temporal and Horizontal Precipitation**
557 **Variability Converge?**
558
559 The addition of the XSAPR2 at the ENA observatory offers new insights into precipitation
560 variability and organization over a domain of 40-60 km radius around the size. However, the
561 XSAPR2 data record is not as long as the KAZR data record which now spans 5 years at the ENA
562 even totaling up to 7.5 years if we consider the Cloud, Aerosols, and Precipitation in the Marine
563 Boundary Layer (CAP-MBL) campaign that took place at the site from April 2009 until January
564 2011 (Wood et al., 2005). Because of their longer data record, profiling radar observations have
565 the potential to inform us about decadal precipitation variability both temporal and structural.
566 However, with vertically pointing observations, it is near impossible to disentangle temporal
567 evolution from horizontal structure. Classical approaches rely on Taylor hypothesis of frozen
568 turbulence to convert elapsed time to horizontal dimension using the horizontal wind speed
569 responsible for advecting cloud and precipitation overhead. While widely used, little research has
570 been conducted to determine the validity and limitations of this assumption (see Oue et al. (2016)
571 for a discussion on cloud fraction). In this section we seek to determine how long does one need
572 to observe precipitation advected overhead to gather statistical precipitation information
573 equivalent to that of an 40 km radius domain.
574
575 Over the 3-month period between 01/10/2018 and 04/01/2018, the domain representativeness of
576 KAZR2 precipitation rate estimates is evaluated using XSAPR2 observations collected over a
577 domain of 40 km radius around the site. Although any height could be used, we perform this
578 comparison at the specific height of 500 m; While KAZR2 precipitation retrievals can be directly
579 extracted at 500 m, those from XSAPR2 must be extracted from gridded CAPPI fields which are
580 constructed following the details provided in Section 6 using a collection of PPI scans. To remove
581 any bias caused by variations in minimum performance of both sensors, a minimum precipitation
582 rate threshold of $10^{-2.8}$ mm hr^{-1} is applied to both sensors reflecting the detectability of the XSAPR2
583 over the selected domain. Statistics for both sensors are estimated using different set averaging
584 time intervals (30 min, 1 h, 3 h, 12 h and 24 h) which allows us to monitor the temporal variability
585 of domain-average precipitation rate. For XSAPR2, using a sliding window, we average all 5-min
586 PPI observations collected during the chosen time interval. For KAZR, we center the time window
587 on the XSAPR2 estimates and average all 2-s observations collected during the chosen time
588 interval.
589
590 Figure 10 shows the precipitation rate pdfs estimated from the XSAPR2 (blue) and KAZR2 (red)
591 for varying averaging time interval. Focusing on features such as the width, the minimum,
592 maximum and modes of the precipitation rate statistical distribution; Results indicate that neither
593 30 min nor 1h averaging of KAZR precipitation rate estimates can be used to replicate the
594 precipitation rate statistics corresponding to those of domain averaged over 30 min (Fig. 10 left
595 column). Averaging of 3 hours of KAZR2 data improves its representativeness of domain average
596 rain rate variabilities on scales of 1 to 3-hrs (2^{nd} and 3^{rd} rows/3^{rd} column). Convergence between

XSAPR2 and KAZR2 time-average precipitation rate estimates is seemingly best when considering the variability of domain-average precipitation rate over 12 h (correlation coefficient R=0.25) or longer timescales; 12-h average domain-average precipitation rate pdf from XSAPR2 and 12-h average precipitation rate pdf from KAZR are similar in both magnitude and mode location.

Although these results are estimated with few observational cases (3 month period), they clearly suggest that XSAPR2 observations are necessary to characterize short-term (< 1 h) domain-average precipitation rate characteristics. They also suggest that longer-term (12 h) domain-average precipitation rate characteristics can be estimated by averaging either XSAPR2 or KAZR2 observations using time-windows of similar lengths.

8.0 Summary and Conclusions

The ARM ENA observatory is the first island-based climate research facility equipped with collocated radars and lidars capable of sampling light oceanic precipitation. Here we presented the characteristics and first light observations from three state-of-the-art 2nd generation radar systems: The Ka-band Zenith radar (KAZR2), the Ka-band scanning ARM cloud radar (KaSACR2) and the X-band scanning ARM precipitation radar (XSAPR2),

One of the initial concerns of operating scanning cloud and precipitation radars over the ocean is the impact of sea-clutter, especially at low-elevation angles. Nearly one hundred hours of clear sky observations were used to characterize the properties of sea-clutter in KaSACR2 and XSAPR2 observations. Analysis of clear and cloudy skies periods and intercomparison of the meteorological and non-meteorological echoes of the KaSACR2 made it possible to design a relatively simple filtering technique to isolate precipitation echoes in XSAPR2 observations. In short, a threshold on normalized coherent power (< 0.3) and on average (5x5 window) cross-correlation (< 0.55), can mitigate second-trip echoes and sea-clutter echoes. Everything considered, we find that XSAPR2 observations collected at 1° elevation, albeit suffering from more clutter contamination than KaSACR2, offer the best compromise between clutter contamination and proximity to the surface.

Measurement calibration is also essential to quantitative precipitation rate retrieval. We applied the Kollias et al. (2019) technique to calibrate the KAZR2 radar reflectivity measurements using Parsivel disdrometer and CloudSat observations. Because they were found to match, the same offset is applied to the KaSACR2 observations. To confirm the recent calibration performed by the ARM engineering team and to explore alternative calibration methods, the XSAPR2 reflectivity measurements were statistically compared to GPM Ku-band radar observations collected around the ENA site. The analysis indicated no noticeable offset; thus, no calibration offset was applied to the XSAPR2. These techniques could be used in the future as a supplement to the ARM radar engineering group efforts to characterize the ENA radars reflectivity measurements.

We capitalized on the availability of closely collected (in both time and physical distance) KAZR2, ceilometer lidar and XSAPR2 measurement to estimate precipitation rate. Precipitation rates retrieved using the O'Connor et al. (2005) radar-lidar technique have the advantage of being

643 estimated with fewer assumptions on the drizzle drop size distribution and can accommodate
644 changes in aerosol loading, liquid water path and evaporation. Unfortunately, for a lack of scanning
645 lidar observations, we cannot apply this technique to scanning radar observations. Instead, we
646 showed how relating the retrieved precipitation rates in the column to radar reflectivity can be used
647 to estimate adaptive (in both time and height) parameters that related observed radar reflectivity
648 (Z) to precipitation rate (R) in the form $Z = \alpha R^{\beta}$. These adaptive parameters can then be applied
649 to retrieve precipitation rate over the domain covered by scanning cloud radars. We report these
650 adaptive parameters for the period between 01/10/2018 and 04/01/2018 which includes the second
651 phase of the ACE-ENA campaign. These adaptive parameters were shown to capture changes in
652 drop size distribution with height as well as temporal changes in the cloud field.
653
654 Throughout this work, comparison of precipitation rate statistics estimated by all three sensors
655 highlighted the following:
656
657 1) Because of strong signal attenuation by gases and liquid at Ka-band, X-band radars are
658 more suited for precipitation mapping especially over large domains.
659 2) When the character of precipitation varies rapidly with height for instance owing to an
660 active evaporation process, zenith-pointing radars are more suited for precipitation
661 characterization;
662 3) However, zenith-pointing observations collected over periods shorter than 12h should not
663 be considered representative of a domain especially one as large as 2,500 km^2 (i.e., ~40 km
664 radius half circle).
665 4) When it comes to capturing the general shape of the precipitation rate distribution, 12-hrs
666 of zenith-pointing radar observations can be averaged to represent the 12-h variability of
667 such a ~40 km radius half circle domain .
668 5) Shorter term domain precipitation rate variability can only be capture by scanning
669 precipitation radars and especially those operating at weakly-attenuating frequencies and
670 with high sensitivity such as the XSAPR2
671 6) Scanning sensors such as the XSAPR2 are also better suited to document sporadic and
672 horizontal homogeneous precipitation including precipitation presenting mesoscale
673 organization.
674
675 In a nutshell, the considerable differences in precipitation rate statistics estimated by the XSAPR2
676 and KAZR2 challenge our ability to objectively estimate precipitation rate statistics over a domain
677 for applications such as evaluation of high-temporal resolution model output. Factors such as
678 instrument sensitivity, sampling resolution, sampling height and domain size should always be
679 considered when comparing model output to observations. One way to consider these factors could
680 be to convert model output rain rates to observable rain rate through the use of forward simulators
681 which can use drop size and atmospheric conditions information to reproduce the attenuation
682 affecting radar signals. Several forward-simulator further take into consideration the dependency
683 of radar sensitivity with range which dictates the minimum detectable rain rate at various distance
684 within a domain (e.g., Tatarevic et al., 2015; Lamer et al., 2018).
685
686
687
688

Authors contributions

K. Lamer coordinated the project, performed the intercomparisons between the precipitation rates produced by the three radars and produced the final manuscript draft. P. Kollias supervised Z. Zhu and B. Puigdomènech Treserras as they respectively analyzed the KAZR2 and both the KaSACR2 and XSAPR2 observations; Analysis steps included performing data post-processing, calibration and precipitation rate retrievals. B. Puigdomènech Treserras also produced the CAPPI part of this work. B. Isom and N. Bharadwaj provided a wealth of information about the radar system characteristics as well as guidance on radar data calibration. All coauthors have read the manuscript draft and have contributed comments.

Acknowledgments

K. Lamer contributions were supported by subcontract 300324 of the Pennsylvania State University with the Brookhaven National Laboratory in support to the U.S. Department of Energy (DOE) ARM-Atmospheric Science Research (ASR) Radar Science group. B. Puigdomènech Treserras contributions were supported through a subcontract with the Brookhaven National Laboratory in support to the ARM-ASR Radar Science group Z. Zhu contributions were supported by the U.S. DOE ASR ENA Site Science award. B. Isom and N. Bharadwaj contributions were supported by Pacific North West National Laboratory. P. Kollias contributions were supported by the U.S. DOE under Contract DE-SC0012704.

Data availability

All ARM data streams are available online at: http://www.archive.arm.gov/discovery/. All GPM data streams are available online at https://pmm.nasa.gov/data-access/downloads/gpm.

References

Adler, R. F., Wang, J.-J., Gu, G., and Huffman, G. J.: A ten-year tropical rainfall climatology based on a composite of TRMM products, Journal of the Meteorological Society of Japan. Ser. II, 87, 281-293, 2009.

Ahlgrimm, M., and Forbes, R.: Improving the representation of low clouds and drizzle in the ECMWF model based on ARM observations from the Azores, Monthly Weather Review, 142, 668-685, 2014.

Alku, L., Moisseev, D., Aittomäki, T., and Chandrasekar, V.: Identification and suppression of nonmeteorological echoes using spectral polarimetric processing, IEEE Transactions on Geoscience and Remote Sensing, 53, 3628-3638, 2015.

Bretherton, C. S., Uttal, T., Fairall, C. W., Yuter, S. E., Weller, R. A., Baumgardner, D., Comstock, K., Wood, R., and Raga, G. B.: The EPIC 2001 stratocumulus study, Bulletin of the American Meteorological Society, 85, 967-978, 2004.

Comstock, K. K., Wood, R., Yuter, S. E., and Bretherton, C. S.: Reflectivity and rain rate in and below drizzling stratocumulus, Quarterly Journal of the Royal Meteorological Society, 130, 2891-2918, 2004.

Comstock, K. K., Bretherton, C. S., and Yuter, S. E.: Mesoscale variability and drizzle in southeast Pacific stratocumulus, Journal of the Atmospheric Sciences, 62, 3792-3807, 2005.

Doviak, R., and Zrnic, D.: Doppler Radar and, 1993.

Ellis, T. D., L'Ecuyer, T., Haynes, J. M., and Stephens, G. L.: How often does it rain over the global oceans? The perspective from CloudSat, Geophysical Research Letters, 36, 2009.

Feingold, G., Koren, I., Wang, H., Xue, H., and Brewer, W. A.: Precipitation-generated oscillations in open cellular cloud fields, Nature, 466, 849, 2010.

Gorgucci, E., Scarchilli, G., and Chandrasekar, V.: Sensitivity of multiparameter radar rainfall algorithms, Journal of Geophysical Research: Atmospheres, 105, 2215-2223, 2000.

Gregers-Hansen, V., and Mital, R.: An empirical sea clutter model for low grazing angles, Radar Conference, 2009 IEEE, 2009, 1-5.

Hogan, R. J.: Fast approximate calculation of multiply scattered lidar returns, Applied Optics, 45, 5984-5992, 2006.

Horst, M., Dyer, F., and Tuley, M.: Radar sea clutter model, Antennas and Propagation, 1978, 6-10.

Iguchi, T., Seto, S., Meneghini, R., Yoshida, N., Awaka, J., and Kubota, T.: GPM/DPR level-2 algorithm theoretical basis document, NASA Goddard Space Flight Center, Greenbelt, MD, USA, Tech. Rep, 2010.

Intrieri, J. M., Stephens, G. L., Eberhard, W. L., and Uttal, T.: A method for determining cirrus cloud particle sizes using lidar and radar backscatter technique, Journal of Applied Meteorology, 32, 1074-1082, 1993.

Kollias, P., Bharadwaj, N., Widener, K., Jo, I., and Johnson, K.: Scanning ARM cloud radars. Part I: Operational sampling strategies, Journal of Atmospheric and Oceanic Technology, 31, 569-582, 2014a.

Kollias, P., Jo, I., Borque, P., Tatarevic, A., Lamer, K., Bharadwaj, N., Widener, K., Johnson, K., and Clothiaux, E. E.: Scanning ARM cloud radars. Part II: Data quality control and processing, Journal of Atmospheric Oceanic Technology, 31, 583-598, 2014b.

Kollias, P., Clothiaux, E. E., Ackerman, T. P., Albrecht, B. A., Widener, K. B., Moran, K. P., Luke, E. P., Johnson, K. L., Bharadwaj, N., and Mead, J. B.: Development and applications of ARM millimeter-wavelength cloud radars, Meteorological Monographs, 57, 17.11-17.19, 2016.

Kollias, P., Puigdomènech Treserras, B., and Protat, A.: Calibration of the 2007-2017 record of ARM Cloud Radar Observations using CloudSat, Atmos. Meas. Tech. Discuss., 2019, 1-30, 10.5194/amt-2019-34, 2019.

Lamer, K., Fridlind, A. M., Ackerman, A. S., Kollias, P., Clothiaux, E. E., & Kelley, M.: $(GO)^2$-SIM: a GCM-oriented ground-observation forward-simulator framework for objective evaluation of cloud and precipitation phase. Geoscientific Model Development, 11(10), 4195-4214. 2018

Lamer, K., Kollias, P., and Nuijens, L.: Observations of the variability of shallow trade wind cumulus cloudiness and mass flux, Journal of Geophysical Research: Atmospheres, 120, 6161-6178, 2015.

Luke, E. P., Kollias, P., Johnson, K. L., and Clothiaux, E. E.: A technique for the automatic detection of insect clutter in cloud radar returns, Journal of Atmospheric and Oceanic Technology, 25, 1498-1513, 2008.

Mather, J., Turner, D., and Ackerman, T.: Scientific maturation of the ARM Program, Meteorological Monographs, 57, 4.1-4.19, 2016.

Matrosov, S. Y.: Attenuation-based estimates of rainfall rates aloft with vertically pointing Ka-band radars, Journal of Atmospheric and Oceanic Technology, 22, 43-54, 2005.

Matrosov, S. Y., Kingsmill, D. E., Martner, B. E., & Ralph, F. M.: The utility of X-band polarimetric radar for quantitative estimates of rainfall parameters. Journal of hydrometeorology, 6(3), 248-262, 2005

Miller, M., and Yuter, S.: Detection and characterization of heavy drizzle cells within subtropical marine stratocumulus using AMSR-E 89-GHz passive microwave measurements, Atmospheric Measurement Techniques, 6, 1-13, 2013.

Moisseev, D. N., and Chandrasekar, V.: Polarimetric spectral filter for adaptive clutter and noise suppression, Journal of Atmospheric and Oceanic Technology, 26, 215-228, 2009.

Moyer, K. A., and Young, G. S.: Observations of mesoscale cellular convection from the marine stratocumulus phase of "FIRE", Boundary-Layer Meteorology, 71, 109-133, 1994.

Nathanson, F. E., Reilly, J. P., and Cohen, M. N.: Radar design principles-Signal processing and the Environment, NASA STI/Recon Technical Report A, 91, 1991.

Nguyen, C. M., Moisseev, D. N., and Chandrasekar, V.: A parametric time domain method for spectral moment estimation and clutter mitigation for weather radars, Journal of Atmospheric and Oceanic Technology, 25, 83-92, 2008.

O'Connor, E. J., Illingworth, A. J., and Hogan, R. J.: A technique for autocalibration of cloud lidar, Journal of Atmospheric and Oceanic Technology, 21, 777-786, 2004.

O'Connor, E. J., Hogan, R. J., and Illingworth, A. J.: Retrieving stratocumulus drizzle parameters using Doppler radar and lidar, Journal of Applied Meteorology, 44, 14-27, 2005.

Oue, M., Kollias, P., North, K. W., Tatarevic, A., Endo, S., Vogelmann, A. M., and Gustafson, W. I.: Estimation of cloud fraction profile in shallow convection using a scanning cloud radar, Geophysical Research Letters, 43, 2016.

Paluch, I., and Lenschow, D.: Stratiform cloud formation in the marine boundary layer, Journal of the atmospheric sciences, 48, 2141-2158, 1991.

Pazmany, A. L., Mead, J. B., Bluestein, H. B., Snyder, J. C., and Houser, J. B.: A mobile rapid-scanning X-band polarimetric (RaXPol) Doppler radar system, Journal of Atmospheric and Oceanic Technology, 30, 1398-1413, 2013.

Rapp, A. D., Lebsock, M., and L'Ecuyer, T.: Low cloud precipitation climatology in the southeastern Pacific marine stratocumulus region using CloudSat, Environmental Research Letters, 8, 014027, 2013.

Rauber, R. M., Stevens, B., Ochs III, H. T., Knight, C., Albrecht, B. A., Blyth, A., Fairall, C., Jensen, J., Lasher-Trapp, S., and Mayol-Bracero, O.: Rain in shallow cumulus over the ocean: The RICO campaign, Bulletin of the American Meteorological Society, 88, 1912-1928, 2007.

Rémillard, J., and Tselioudis, G.: Cloud regime variability over the Azores and its application to climate model evaluation, Journal of Climate, 28, 9707-9720, 2015.

Rosenkranz, P. W.: Water vapor microwave continuum absorption: A comparison of measurements and models, Radio Science, 33, 919-928, 1998.

Ryzhkov, A., Zhang, P., Doviak, R., and Kessinger, C.: Discrimination between weather and sea clutter using Doppler and dual-polarization weather radars, Proc. 27th General Assembly of the International Union of Radio Science, 3, 2002.

Savic-Jovcic, V., and Stevens, B.: The structure and mesoscale organization of precipitating stratocumulus, Journal of the Atmospheric Sciences, 65, 1587-1605, 2008.

Schumacher, C., and Houze Jr, R. A.: Comparison of radar data from the TRMM satellite and Kwajalein oceanic validation site, Journal of Applied Meteorology, 39, 2151-2164, 2000.

Sharon, T. M., Albrecht, B. A., Jonsson, H. H., Minnis, P., Khaiyer, M. M., van Reken, T. M., Seinfeld, J., and Flagan, R.: Aerosol and cloud microphysical characteristics of rifts and gradients in maritime stratocumulus clouds, Journal of the Atmospheric Sciences, 63, 983-997, 2006.

Siggia, A., and Passarelli, R.: Gaussian model adaptive processing (GMAP) for improved ground clutter cancellation and moment calculation, Proc. ERAD, 2004, 421-424.

Stevens, B., Lenschow, D. H., Vali, G., Gerber, H., Bandy, A., Blomquist, B., Brenguier, J.-L., Bretherton, C., Burnet, F., and Campos, T.: Dynamics and chemistry of marine stratocumulus—DYCOMS-II, Bulletin of the American Meteorological Society, 84, 579-594, 2003.

Stevens, B., Vali, G., Comstock, K. K., Wood, R., Van Zanten, M. C., Austin, P. H., Bretherton, C. S., and Lenschow, D. H.: Pockets of open cells and drizzle in marine stratocumulus, Bulletin of the American Meteorological Society, 86, 51-58, 2005.

Stevens, B., Farrell, D., Hirsch, L., Jansen, F., Nuijens, L., Serikov, I., Brügmann, B., Forde, M., Linne, H., and Lonitz, K.: The Barbados Cloud Observatory: Anchoring investigations of clouds and circulation on the edge of the ITCZ, Bulletin of the American Meteorological Society, 97, 787-801, 2016.

Tatarevic, A., Kollias, P., Oue, M., & Wang, D.: User's Guide CR-SIM SOFTWARE v 3.0. McGill University Clouds Research Group, Document available at http://radarscience. weebly. com/radar-simulators. html. Last accessed 07/2019

Torres, S. M., and Zrnic, D. S.: Ground clutter canceling with a regression filter, Journal of Atmospheric and Oceanic Technology, 16, 1364-1372, 1999.

Toyoshima, K., Masunaga, H., and Furuzawa, F. A.: Early evaluation of Ku-and Ka-band sensitivities for the global precipitation measurement (GPM) dual-frequency precipitation radar (DPR), Sola, 11, 14-17, 2015.

Unal, C.: Spectral polarimetric radar clutter suppression to enhance atmospheric echoes, Journal of atmospheric and oceanic technology, 26, 1781-1797, 2009.

875 Vali, G., Kelly, R. D., French, J., Haimov, S., Leon, D., McIntosh, R. E., and Pazmany, A.:
876 Finescale structure and microphysics of coastal stratus, Journal of the Atmospheric
877 Sciences, 55, 3540-3564, 1998.

878 VanZanten, M., Stevens, B., Vali, G., and Lenschow, D.: Observations of drizzle in nocturnal
879 marine stratocumulus, Journal of the Atmospheric Sciences, 62, 88-106, 2005.

880 Villarini, G., and Krajewski, W. F.: Review of the different sources of uncertainty in single
881 polarization radar-based estimates of rainfall, Surveys in Geophysics, 31, 107-129, 2010.

882 Wang, H., and Feingold, G.: Modeling mesoscale cellular structures and drizzle in marine
883 stratocumulus. Part I: Impact of drizzle on the formation and evolution of open cells,
884 Journal of the Atmospheric Sciences, 66, 3237-3256, 2009.

885 Warren, R. A., Protat, A., Siems, S. T., Ramsay, H. A., Louf, V., Manton, M. J., and Kane, T. A.:
886 Calibrating ground-based radars against TRMM and GPM, Journal of Atmospheric and
887 Oceanic Technology, 35, 323-346, 2018.

888 Wood, R.: Drizzle in stratiform boundary layer clouds. Part II: Microphysical aspects, Journal of
889 the Atmospheric Sciences, 62, 3034-3050, 2005.

890 Wood, R., and Hartmann, D. L.: Spatial variability of liquid water path in marine low cloud: The
891 importance of mesoscale cellular convection, Journal of Climate, 19, 1748-1764, 2006.

892 Wood, R., Bretherton, C., Leon, D., Clarke, A., Zuidema, P., Allen, G., and Coe, H.: An aircraft
893 case study of the spatial transition from closed to open mesoscale cellular convection over
894 the Southeast Pacific, Atmospheric Chemistry and Physics, 11, 2341, 2011.

895 Wood, R.: Stratocumulus clouds, Monthly Weather Review, 140, 2373-2423, 2012.

896 Yamaguchi, T., and Feingold, G.: On the relationship between open cellular convective cloud
897 patterns and the spatial distribution of precipitation, Atmospheric Chemistry and Physics,
898 15, 1237, 2015.

899 Yang, F., Luke, E. P., Kollias, P., Kostinski, A. B., and Vogelmann, A. M.: Scaling of drizzle virga
900 depth with cloud thickness for marine stratocumulus clouds, Geophysical Research Letters,
901 45, 3746-3753, 2018.

902 Yuter, S. E., Serra, Y. L., and Houze Jr, R. A.: The 1997 Pan American climate studies tropical
903 eastern Pacific process study. Part II: Stratocumulus region, Bulletin of the American
904 Meteorological Society, 81, 483-490, 2000.

905 Zhou, X., Heus, T., and Kollias, P.: Influences of drizzle on stratocumulus cloudiness and
906 organization, Journal of Geophysical Research: Atmospheres, 122, 6989-7003, 2017.

907 Zhou, X., Ackerman, A. S., Fridlind, A. M., and Kollias, P.: Simulation of Mesoscale Cellular
908 Convection in Marine Stratocumulus. Part I: Drizzling Conditions, Journal of the
909 Atmospheric Sciences, 75, 257-274, 2018.

Tables

Table 1 Specification of ARM ENA zenith and scanning second generation radars

	KAZR2		KaSACR2		XSAPR2	
Frequency (MHz)	34860		35290		9500	
Peak power (kW)	2.2		2.2		300	
Maximum Duty cycle (%)	5.0		5.0		0.1	
Pulse compression	Yes		Yes (but not on)		No	
Pulse length	4 μs	200 ns	?		0.66 μs	
Sensitivity single pulse (dBZ)	-32.5 (at 1 km)	-44 (at 1 km)	-15 (at 20 km)		-21 (at 20 km)	
Dead zone (m)	72	737	400		100	
Unambiguous range (km)	18		40		Over 100	
Gate spacing (m)	30		30		100	
Antenna size (m)	1.82		1.82		5.0	
3-dB Beam width (°)	0.3		0.3		0.45	
Scan rate (° s^{-1})	-		3		6	
Scan strategy	Zenith		PPI scan		VCP scan	
Elevation angle (°)	90		0.5		0 to 5 every 0.5	
Azimuthal sector (°)	-		360		160	
Scan time	3 s		2 min		5 min	
Scan Interval	Continuous		15 min			
Transmit polarization	H		Alternating H and V		Simultaneous H and V	
Received polarization	H and V		H and V		H and V	
Amplifier Type	Klystron (EIKA)		Klystron (EIKA)		Magnetron	
Signal processing	FFT		Pulse-pair	FFT	Pulse-pair	FFT
Doppler spectra	Yes		No	Yes	No	Yes
Second trip echo removal technique	Challenging		Frequency Hopping	Challenging	None Coherent Power technique	
Velocity dealiasing technique	Challenging		Staggered Pulse Repetition Time	Challenging	Challenging	

Figures

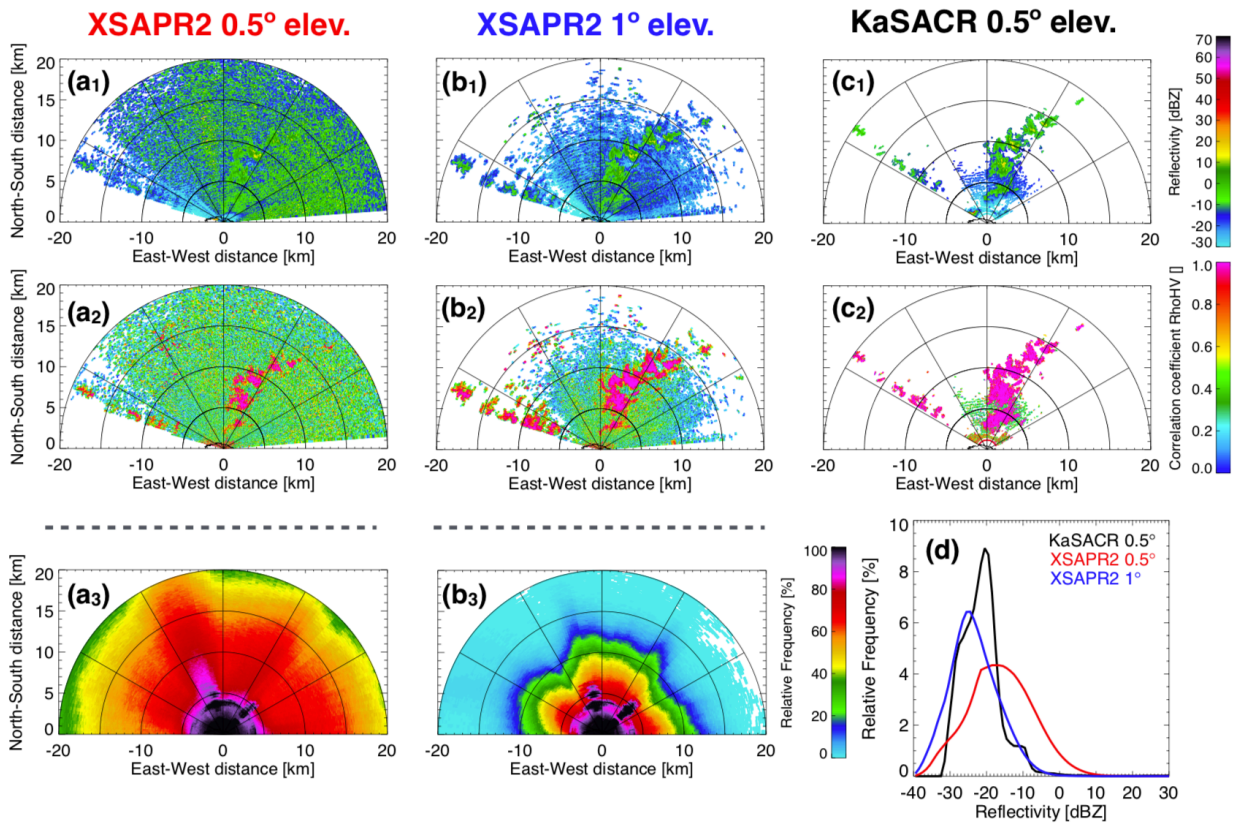

Figure 1. For significant echoes, 1) radar reflectivity, 2) correlation coefficient (ρ_{HV}) and 3) relative frequency of occurrence of clutter as observed by the a) XSAPR2 at 0.5° elevation, b) XSAPR2 at 1° elevation and c) KaSACR at 0.5° elevation. d) Clutter characteristics estimated using 93 hours of clear sky observations.

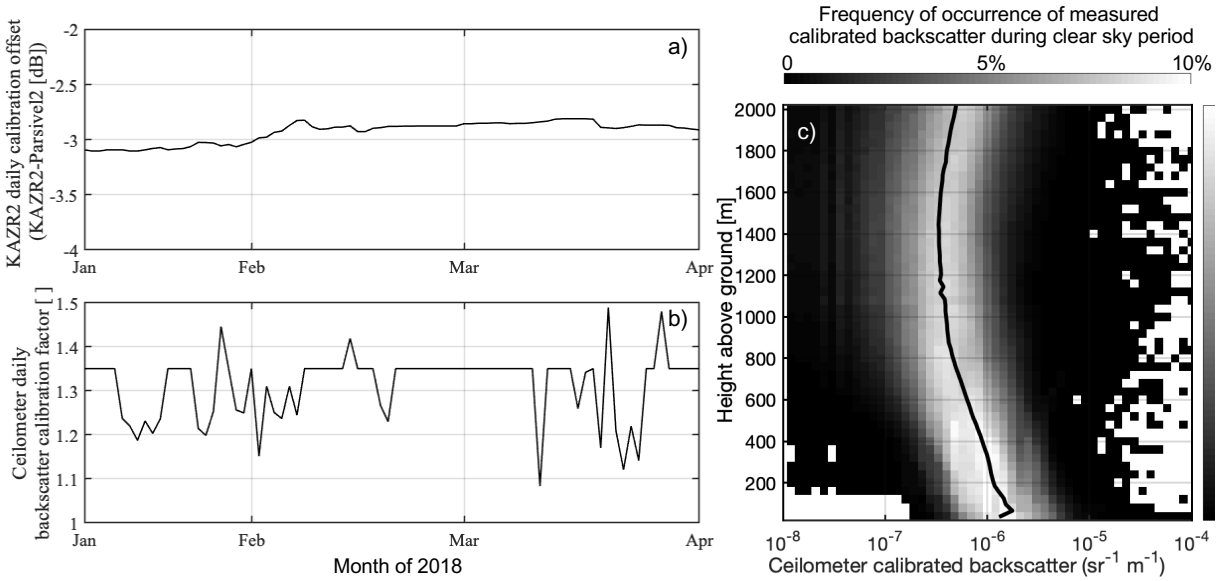

Figure 2. a) Ka-band Zenith Radar (KAZR) calibration offset to be removed from the KAZR radar reflectivity in order to match Parsivel Disdrometer radar reflectivity estimates. b) Ceilometer lidar calibration factor to be multiplied to observed backscatter to match theoretical liquid cloud lidar ratios. c) Frequency of occurrence of observed backscatter during clear sky conditions, solid black line is interpreted as the mean aerosol backscatter signal, observations small than this threshold at each height are eliminated from the drizzle analysis.

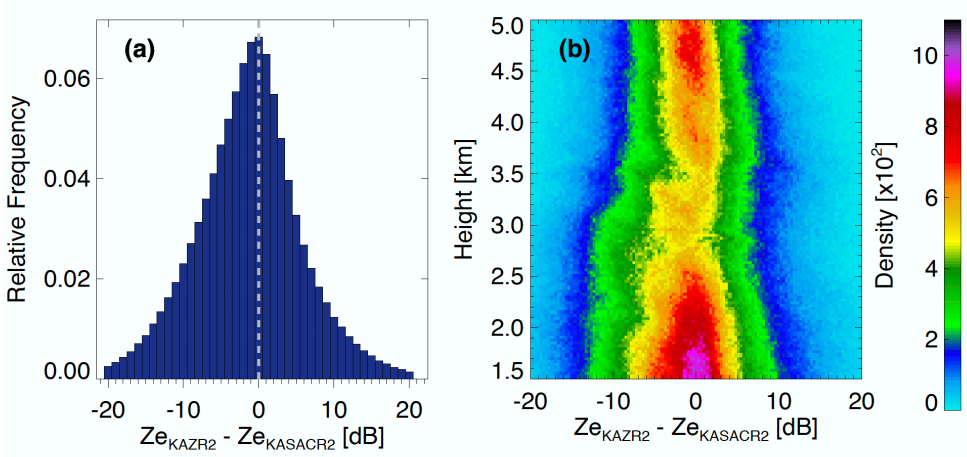

Figure 3. For period when KAZR2 and KaSACR2 are matched in time and range a) Difference in radar reflectivity reported by both sensors over the ranges between 1.5 and 5.0 km, b) Difference in radar reflectivity reported by both sensors as a function of range.

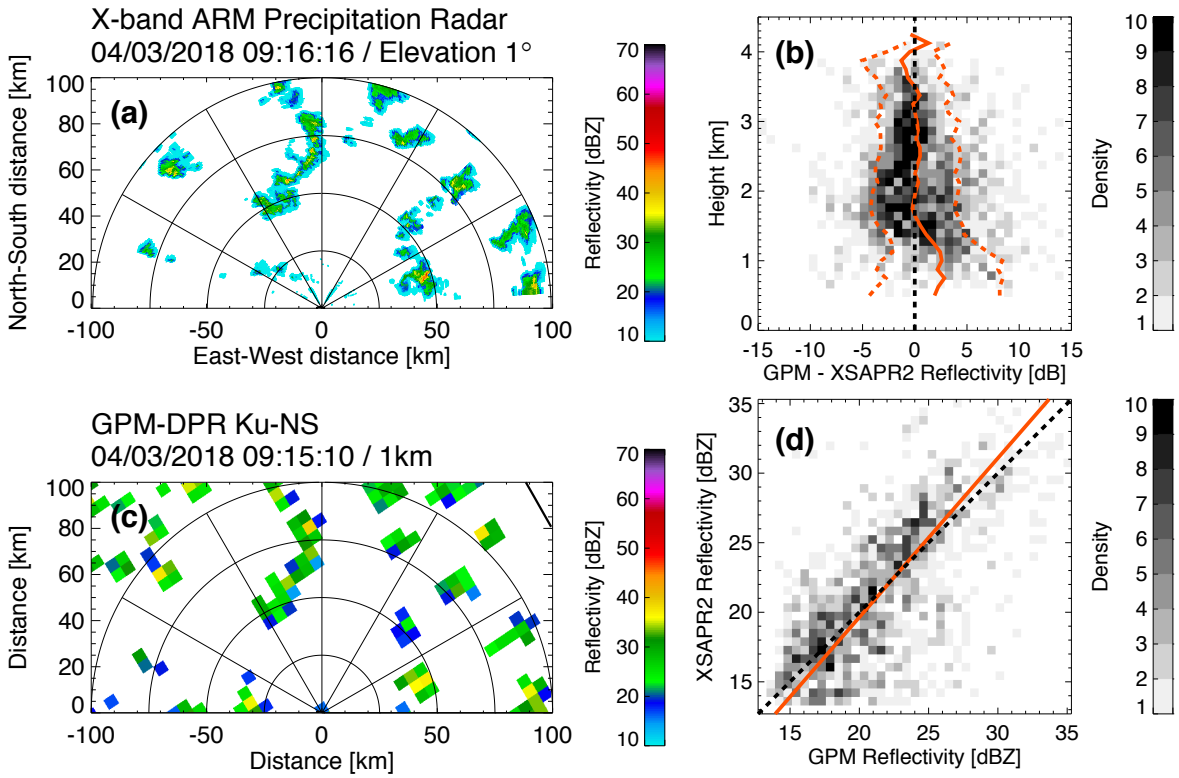

Figure 4. For the conditions that occurred on 04/03/2018 around 09:15 as observed by a) XSAPR2 radar reflectivity at 1° elevation and c) GPM-DPR Ku-band radar reflectivity at 1 km height. For the entire geometry-matching dataset with 1516 points used for the calibration b) Scatter, mean (orange) and standard deviation (dashed lines) of the difference between the GPM-DPR Ku-band and XSAPR2 radar reflectivity measurements as a function of height and d) scatterplot comparing the XSAPR2 and GPM-DPR Ku-band reflectivities measurements above the GPM surface echo height of 1.5 km; Also plotted is the 1-to-1 relationship (dashed line) and the best linear fit to the observations (solid orange line).

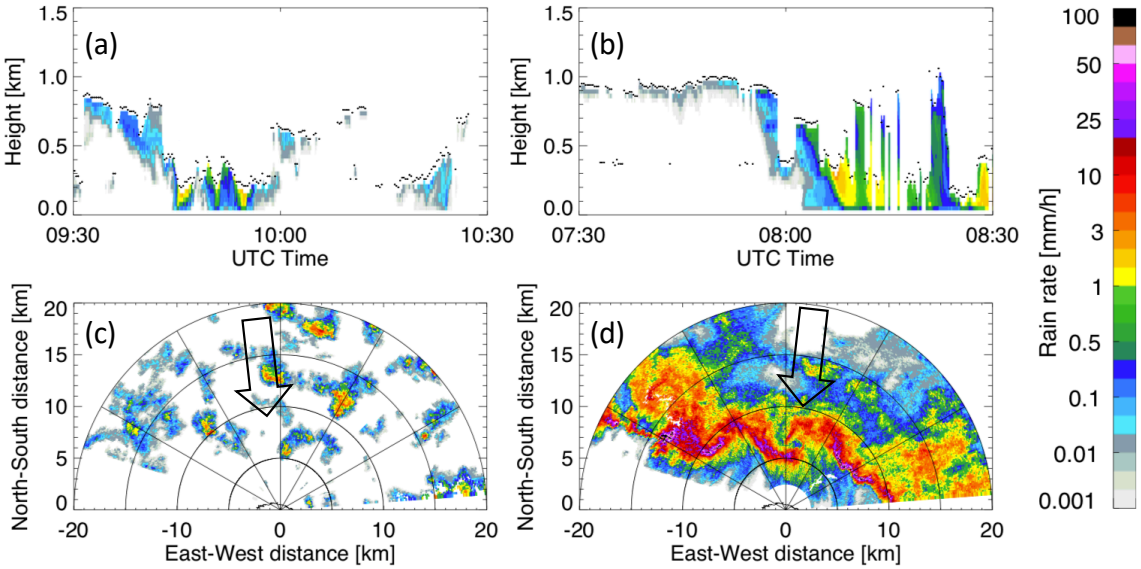

Figure 5. Retrieval of popcorn convection precipitation rate on 02/02/2018 using a) KAZR2 (zenith between 9:30 to 10:30 UTC) and c) KaSACR2 (1° elevation PPI at 10:00 UTC). Retrieval of squall line precipitation rate on 02/03/2018 using b) KAZR2 (zenith between 7:30 to 8:30 UTC) and d) KaSACR2 (1° elevation PPI at 8:00 UTC). Also indicated are the location of cloud bases (black dots in panels a-b) and the general wind direction (arrows in panels c-d). Note that KAZR2 is located at (0 km,0 km).

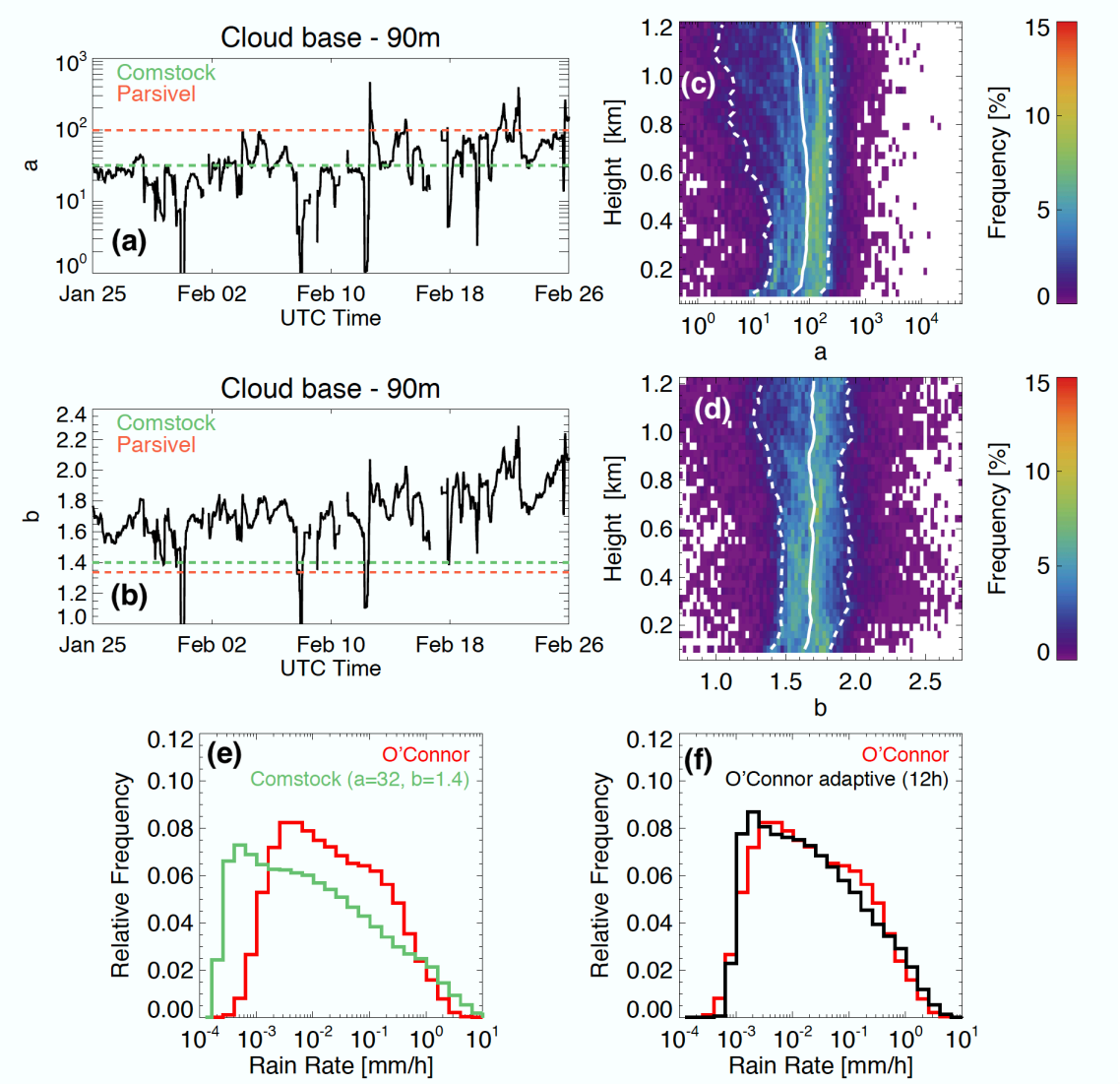

963 **Figure 6.** Time series of the α (a) and β (b) coefficients used to estimate precipitation rate 90
964 m below cloud base height for a 30-day long period that overlaps with the second phase of the
965 ACE-ENA field campaign. For the same time period, distribution of the α (c) and β (d)
966 coefficients with height along with their median (solid line) and 25th and 75th percentile values
967 (dashed line). Precipitation rate distributions retrieved using the O'Connor et al. (2005)
968 technique (red) and estimated using the adaptive coefficients (f, black) or the fixed coefficients
969 proposed by *Comstock et al.*, [2004] (e, green). *Comstock et al.*, [2004] coefficients and
970 coefficients determined from disdrometer observations are both presented in panels a and b
971 using dashed green lines and orange lines respectively.
972
973

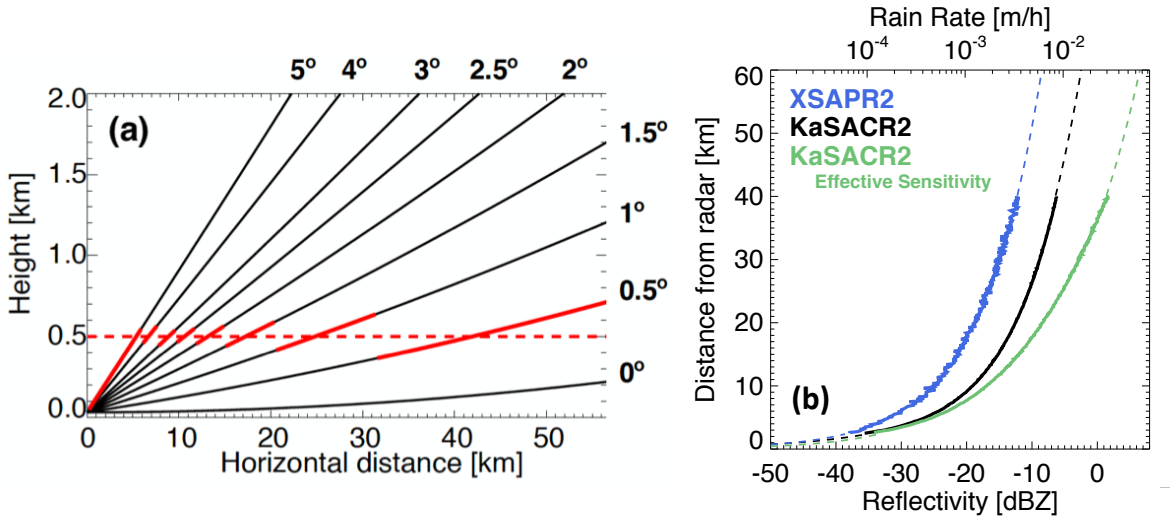

Figure 7. a) PPI scan geometry and b) Theoretical sensitivity of the XSAPR2 (blue) and KaSACR2 (black) along with the KaSACR2 "effective" sensitivity considering it is affected by gas attenuation (green).

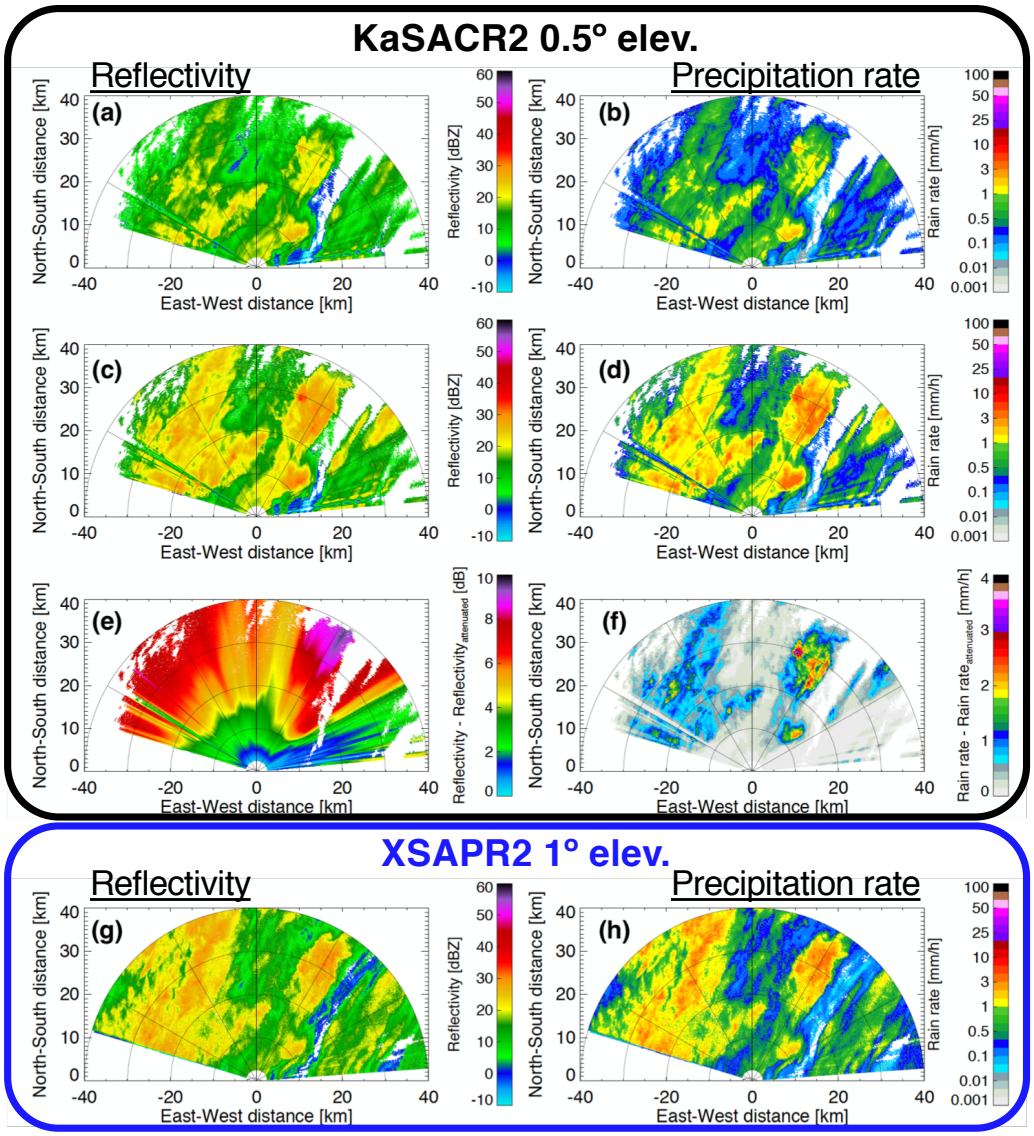

Figure 8. Example of observations/retrievals of the conditions happening on 02/13/2018 at 00:10 UTC. Shown for KaSACR2 perfoming 0.5° elevation PPI a) radar reflectivity field corrected for gaseous attenuation neglecting liquid water attenuation and b) corresponding precipitation rate retrieved using adaptive Z-R relationships; c) radar reflectivity field corrected for both gas and liquid water attenuation and d) corresponding precipitation rate; e) difference between a and c showing the range-accumulated radar reflectivity liquid water attenuation correction and f) the corresponding precipitation rates bias. The bottom panels (g) and (h) show simulataneously collected XSAPR2 1.0° PPI observations for reference.

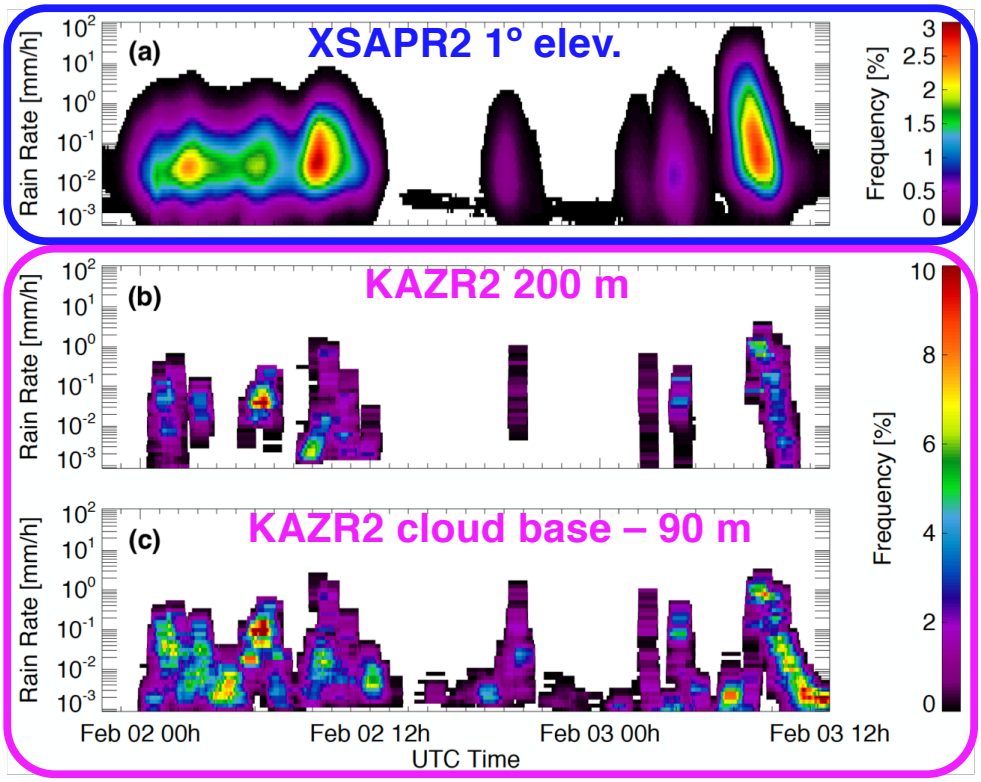

Figure 9. For a 36-h period (00:00 UTC February 2 to 12:00 UTC February 3), hourly probability density functions (pdfs) of precipitation rate estimated from a) XSARP2 when performing a 1 ° elevation PPI scan, b) KAZR2 200 m from the surface and c) KAZR2 90 m below cloud base height

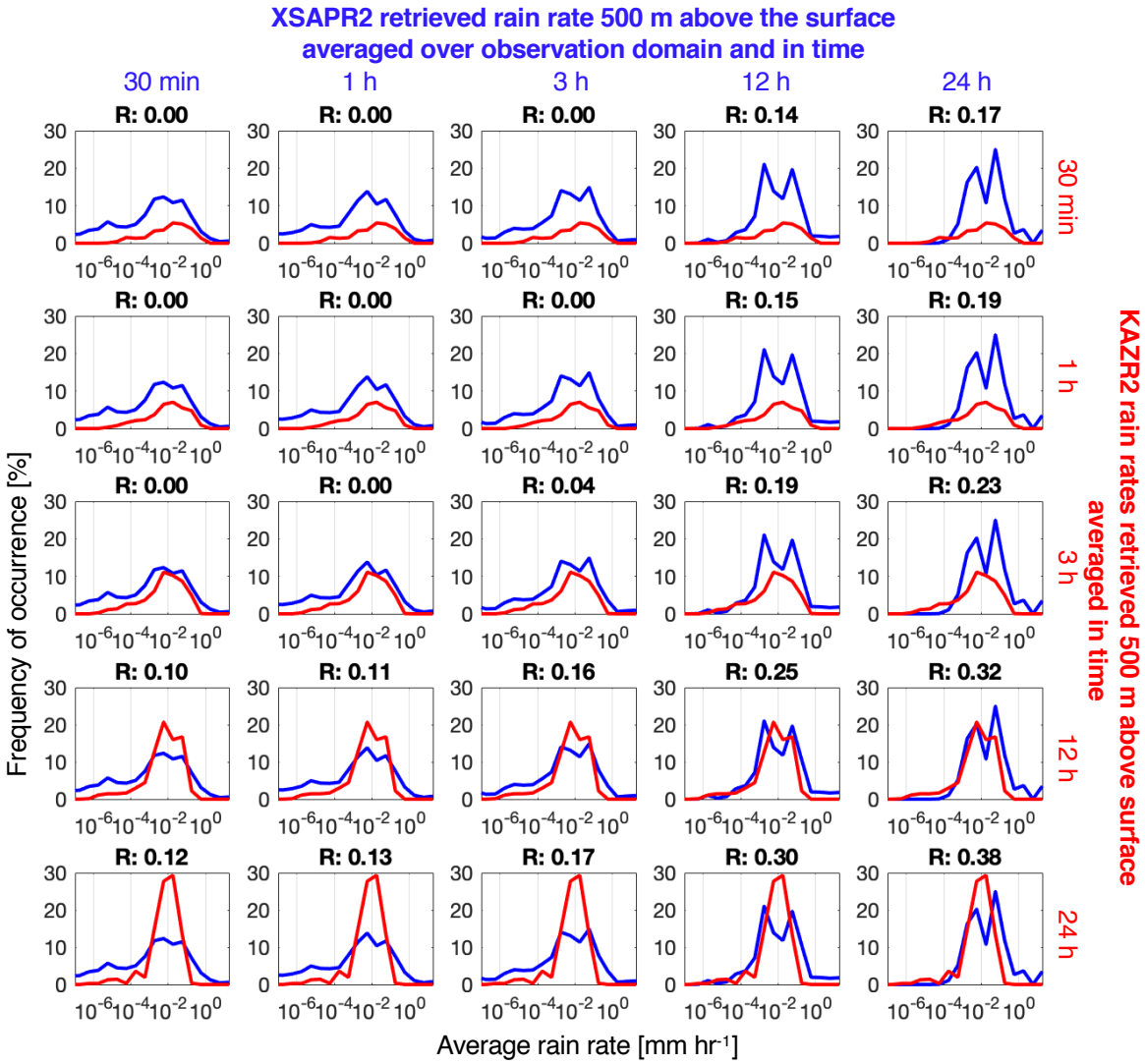

Figure 10. Probability density function of average (over different time windows) precipitation rate as estimated the XSAPR2 and by the KAZR2 (red) both at 500 m above the surface in $10^{0.5}$ mm hr^{-1} bins; The XSAPR2 precipitation rates 500 m above the surface being from gridded CAPPI constructed using a collection of PPI scans and are limited to the domain between 2.5 and 40 km around the location of the KAZR2. Over each box is the correlation coefficient (R) between the XSAPR2 and the KAZR2 average precipitation rates.